**ORIGINAL ARTICLE / ÖZGÜN MAKALE**

# AN *IN SILICO* PHARMACOKINETIC INVESTIGATION OF ORGANIC LUMINOGENS: UNDERSTANDING THE NIR AIEGENS AND THEIR INTERACTIONS WITH SERUM ALBUMINS

## ORGANİK LUMİNOJENLERİN İN SİLİKO FARMAKOKİNETİK İNCELENMESİ: NIR AIEJENLERİ VE SERUM ALBÜMİNLERİ İLE ETKİLEŞİMLERİNİ ANLAMAK

**Harun NALÇAKAN[1]** (ID), **Gülbin KURTAY[2]*** (ID), **Dilara Tuğçe ÖZDİL[1]** (ID), **Züleyha YILMAZ[1]** (ID)

[1]Ankara University, Faculty of Sciences, Department of Chemistry, 06100, Ankara, Türkiye
[2]Hacettepe University, Faculty of Sciences, Department of Chemistry, 06800, Ankara, Türkiye

## ABSTRACT

**Objective:** *Fluorescence imaging (FLI) is accepted as a highly effective method for visualizing bioanalytics directly and gaining insight into complicated biological structures and processes. In this context, newly tailored organic molecules, which have the potential to be used in FLI, especially near-infrared (NIR) regions supported by aggregation-induced emission luminogens (AIEgens), are a rapidly developing area of study. Herein, using ADMET and molecular docking analyses, we examined the pharmacokinetic properties of both model ($D_2$-$A_2$-$D_2$) and newly designed ($D_n$-$A_n$-$D_n$) organic luminogens to interact with blood proteins, namely bovine serum albumin (BSA) and human serum albumin (HSA), which have emerged as a versatile carrier of several therapeutic agents against preliminary cancer and infectious diseases.*

**Material and Method:** *The structural properties of the examined luminogens were computed using the Gaussian 09 software package. The DFT/B3LYP/6-31G(d,p) level was then utilized for geometry optimization and accurately determining electronic structures and molecular properties. Lipinski's rule of five was applied to predict the drugability of the compounds using the SwissADME web tool. Molinspiration was used for further validation of these properties and additional bioactivity parameters. Toxicity parameters were evaluated with OSIRIS Property Explorer (v.4.5.1). Molecular docking simulations of the luminogen-albumin complexes were performed using SAMSON 2022 R2 modeling platform and implemented Autodock-vina extension. The X-ray crystal structures of bovine serum albumin (BSA, PDB ID: 4F5S) and human serum albumin (HSA, PDB ID: 4L9Q) were obtained from the Protein Data Bank. Visualization of the docking interactions was conducted using Discovery Studio Visualizer 2021.*

**Result and Discussion:** *The compounds $D_1$-$A_1$-$D_1$ and $D_1$-$A_4$-$D_1$ stood out concerning molecular weight (MW) and ClogP$_{o/w}$ values, making them promising candidates for drug design. An analysis of lipophilicity revealed that these two compounds displayed high miLogP values, indicating a high degree of lipophilicity, which is generally beneficial for drug delivery. They also exhibited moderate bioactivity based on GPCR ligand and protease inhibitor (PI) parameters. On the other hand, $D_4$-$A_3$-$D_4$ showcased paramount interaction with bovine serum albumin (BSA), while $D_5$-$A_3$-$D_5$ demonstrated the highest binding affinity with human serum albumin (HSA).*

**Keywords:** *ADMET, AIEgen, BSA, HSA, molecular docking*

---

* **Corresponding Author / Sorumlu Yazar:** Gülbin Kurtay
 **e-mail / e-posta:** gulbinkurtay@hacettepe.edu.tr, **Phone / Tel.:** +903122977940

## ÖZ

**Amaç:** *Floresans görüntüleme (FLI), biyoanalitikleri doğrudan görselleştirme ve karmaşık biyolojik yapıları ve süreçleri anlamak için son derece etkili bir yöntem olarak kabul edilir. Bu bağlamda, özellikle agregasyon-indüklü emisyon luminojenleri (AIEjen) tarafından desteklenen ve yakın kızılötesi (NIR) bölgede kullanılma potansiyeli olan yeni özelleştirilmiş organik moleküller, hızla gelişen bir çalışma alanıdır. Bu noktada, ADMET ve moleküler kenetlenme analizlerini kullanarak, hem model ($D_2$-$A_2$-$D_2$) hem de yeni tasarlanmış ($D_n$-$A_n$-$D_n$) organik luminogenlerin kan proteinleri ile etkileşme özelliklerini farmakokinetik açıdan inceledik. Bu kan proteinleri, özellikle sığır serum albumini (BSA) ve insan serum albumini (HSA), erken kanser ve bulaşıcı hastalıklarla mücadelede çeşitli terapötik ajanların taşıyıcısı olarak öne çıkmıştır.*

**Gereç ve Yöntem:** *İncelenen luminojenlerin yapısal özellikleri Gaussian 09 yazılım paketi kullanılarak hesaplandı. Daha sonra DFT/B3LYP/6-31G(d,p) seviyesi, geometri optimizasyonu ve elektronik yapıların ve moleküler özelliklerin doğru bir şekilde belirlenmesi için kullanıldı. Bileşiklerin ilaçlaştırılabilirliğini tahmin etmek için Lipinski'nin beşli kuralı SwissADME web aracı kullanılarak uygulandı. Bu özelliklerin ve ek biyoaktivite parametrelerinin daha fazla doğrulanması için Molinspiration kullanıldı. Toksisite parametreleri OSIRIS Property Explorer (v.4.5.1) ile değerlendirildi. Luminojen-albümin komplekslerinin moleküler kenetlenme simülasyonları SAMSON 2022 R2 modelleme platformu ve Autodock-vina uzantısı kullanılarak gerçekleştirildi. Sığır serum albümininin (BSA, PDB ID: 4F5S) ve insan serum albümininin (HSA, PDB ID: 4L9Q) X-ışını kristal yapıları Protein Data Bank'tan alındı. Bağlanma etkileşimlerinin görselleştirilmesi Discovery Studio Visualizer 2021 kullanılarak gerçekleştirildi.*

**Sonuç ve Tartışma:** *$D_1$-$A_1$-$D_1$ ve $D_1$-$A_4$-$D_1$ bileşikleri, moleküler ağırlık (MA) ve Clog$P_{o/w}$ değerleri açısından öne çıkarak onları ilaç tasarımı için umut verici adaylar haline getirdi. Lipofilisite analizi, bu iki bileşiğin yüksek miLogP değerleri gösterdiğini ortaya çıkardı ki bu genellikle ilaç taşınım için istenen yüksek derecede lipofilikliğe işaret etmektedir. Ayrıca bu bileşikler, GPCR ligandı ve proteaz inhibitörü (PI) parametrelerine dayalı olarak da orta düzeyde biyoaktivite sergilediler. Öte yandan $D_4$-$A_3$-$D_4$, sığır serum albümini (BSA) ile olağanüstü etkileşim sergilerken, $D_5$-$A_3$-$D_5$, insan serum albümini (HSA) ile en yüksek bağlanma afinitesini gösterdi.*

**Anahtar Kelimeler:** *ADMET, AIEjen, BSA, HSA, moleküler kenetlenme*

## INTRODUCTION

Cancer, characterized by the abnormal and uncontrolled growth of human cells, encompasses the development of tumors. The process of metastasis, whereby cancer cells spread to distant locations within the body, is a well-known feature of the advanced stages of the disease [1]. Metastatic cancer has increasingly posed a grave threat to public health, constituting a significant ailment affecting humankind [2]. Medicine has developed and implemented various diagnostic and treatment techniques to tackle cancer's many forms and stages. These include surgical procedures, chemotherapy, radiation treatment, immunotherapy, and hormone therapy [3-5]. While these cancer treatments offer potential benefits, it is crucial to recognize that they can also lead to significant side effects, potentially causing harm to healthy tissues or organs [6-8].

For this reason, fluorescence imaging (FLI)-assisted photodynamic therapy (PDT) has gained significant attention as a promising alternative to conventional treatment methods. This approach offers several advantages, including minimizing long-lasting side effects, precise monitoring of drug distribution, tumor visualization, spatial and temporal specificity, and minimally invasive treatment [9-12]. PDT operates through a mechanism wherein specially formulated photoactive materials, referred to as photosensitizers (PSs), are photoexcited by light of a specific wavelength. These PSs can follow two distinct photodynamic reaction pathways, namely type I and type II, resulting in the production of highly cytotoxic reactive oxygen species (ROS) or singlet oxygen ($^1O_2$), respectively [13,14]. The induction of either apoptotic (programmed) or necrotic (non-programmed) cell death in malignantly proliferating cells is a consequence of the cytotoxic species generated through these reaction pathways [15-17].

Photosensitizers (PSs) are activated through photochemical processes, allowing them to enter an excited state. This activation can be achieved using different light sources, including those within the

visible and near-infrared (NIR) spectrum, which is particularly desirable for PS activation [18,19]. Hence, the current focus lies in advancing photosensitizers that exhibit emission in the near-infrared (NIR) region. This choice of wavelength facilitates improved penetration efficiency, especially in deep tissues, thereby enabling efficient eradication of tumor cells [20]. It is worth highlighting that conventional imaging techniques, operating within the 400-700 nm emission range, exhibit a limited tissue penetration depth. Furthermore, the imaging quality of deep tissues is often considered inadequate in the first near-infrared (NIR-I) region, spanning 700-900 nm. As a result, recent research endeavors have concentrated on developing photosensitizers that emit in the second near-infrared (NIR-II) region, spanning 1000 to 1700 nm.

The utilization of the NIR-II region offers an enhanced depth of penetration and improved spatial-temporal resolution, leading to superior monitoring quality in biological imaging [21-24]. The design of an appropriate photosensitizer for photodynamic therapy requires meticulous consideration of the compound's structure. One crucial aspect is attaining a high photoluminescence quantum yield (PLQY) to enable substantial emission within the desired region of the electromagnetic spectrum [25]. Challenges arise in the design of photosensitizers, notably due to the occurrence of aggregation-caused quenching (ACQ) effect arising from strong intermolecular π-π interactions. This effect significantly reduces the PLQY of the photosensitizer, ultimately impacting tissue penetration efficiency.

Researchers have focused on various luminogens that exhibit aggregation-induced emission (AIE) properties to tackle these challenges. Furthermore, several types of fluorophores capable of generating near-infrared (NIR-II) emissions have also garnered interest. These include quantum dots (QDs), carbon nanotubes, rare earth materials, and organic fluorophores [26]. Organic fluorophores possess outstanding designability regarding their physical and optical characteristics, minimal biotoxicity, *in vivo* biocompatibility, and biodegradability. These attributes render them the optimal choice with immense potential for clinical translation, making them highly suitable for various biomedical applications [27,28]. Recently, attention has turned to using aggregation-induced luminogens (AIEgens) as a potential solution. AIEgens employ twisted structures that effectively minimize intermolecular π-π interactions, enhancing photoluminescence properties [29-32].

Cheng's group has made remarkable contributions to the exploration of donor-acceptor-donor (D-A-D) type AIEgens, which have gained prominence as a notable source of near-infrared (NIR-II) emissions [33]. The design strategy employed for D-A-D luminogens is based on the premise that a reduced energy gap between the highest occupied molecular orbital (HOMO) and the lowest unoccupied molecular orbital (LUMO) leads to emission at longer wavelengths. Thus, extending the π-conjugation length in photosensitizers is a favorable approach to decreasing the band gap value [34]. Carrying out this strategy for developing organic fluorophores in the NIR-II region presents more significant challenges than visible light emitters.

The alternative solution involves constructing electron donors (D) to elevate the HOMO level and electron acceptors (A) to reduce the LUMO level. Consequently, the majority of NIR-II AIEgens are constructed by reinforcing the donor and acceptor units [35]. P. Xu et al. successfully synthesized a novel near-infrared (NIR-II) emitter exhibiting AIE characteristics. The design of the emitter involved incorporating a triphenylamine fragment as the electron donor (D), along with tetraphenylethene as a molecular rotor, onto a benzobisthiadiazole (BBT) unit serving as the electron acceptor (A). It is worth noting that BBT is a commonly utilized building block for NIR dyes [36].

Extensive scientific efforts have been dedicated to studying the complex interactions between human serum albumin (HSA) and bovine serum albumin (BSA) with a variety of dye molecules. An example of this is the triphenylmethane dye, Brilliant Green, which demonstrated a remarkable 300-fold increase in fluorescence when it was bound to Bovine Serum Albumin (BSA) in the presence of the macrocyclic host cucurbituril (CB7). This observation highlights the cooperative binding behavior between the dye and BSA, as well as the crucial role played by CB7 in enhancing the binding affinity [37].

Anees et al. conducted a notable investigation on the interaction between NIR-I dye molecules and HSA and BSA, demonstrating their potential utility as protein sensors [38]. The study emphasized the phenomenon of self-assembly shown by near-infrared (NIR-I) dye molecules, which resulted in the formation of nanoparticles. This self-assembly process occurred in the presence of human serum

albumin (HSA) or bovine serum albumin (BSA), resulting to an increase in fluorescence emission and the ability to selectively bind to proteins. The accurate detection and quantification of proteins can be achieved by the subsequent changes in fluorescence characteristics that occur upon dye attachment. This highlights the promise of near-infrared dye-protein interactions for applications in protein sensing.

Additionally, the study conducted by Jameson et al. investigated the interaction between near-infrared II (NIR-II) dye molecules and human serum albumin (HSA) and bovine serum albumin (BSA) for the purpose of bioimaging applications [39]. The findings of this work demonstrate the successful encapsulating of near-infrared-II (NIR-II) dye molecules within nanoparticles that are biocompatible. These nanoparticles were then coupled to human serum albumin (HSA) or bovine serum albumin (BSA). The dye-protein complexes that were obtained exhibited heightened fluorescence emission in the near-infrared II (NIR-II) region, hence opening up possibilities for the advancement of deep tissue imaging. The enhanced stability and pharmacokinetic properties of these dye nanoparticles were ascribed to their interaction with proteins, highlighting the promise of near-infrared II (NIR-II) dye-protein interactions in the field of advanced bioimaging and theragnostic applications.

Furthermore, the researchers investigated the interaction between NIR-I dye molecules and human serum albumin (HSA) and bovine serum albumin (BSA) in order to assess their potential as photothermal agents in the field of cancer therapy [40]. The present study showcased the creation of enduring dye-protein complexes that, when subjected to near-infrared (NIR-I) laser radiation, displayed effective conversion of light into heat energy. Consequently, this phenomenon resulted in the generation of localized heat, ultimately leading to the specific eradication of tumor cells. This highlights the promising prospects of near-infrared dye-protein interactions in the development of groundbreaking photothermal therapies.

In conclusion, the literature provides an in-depth understanding of the multifaceted interactions between dye molecules and serum albumins, elucidating the underlying binding mechanisms, fluorescence enhancement phenomena, and potential applications of these interactions in a variety of scientific domains ranging from chemistry and medicine to diagnostics and therapeutics.

In this study, a detailed quantum chemical, ADMET and molecular docking investigation was conducted to reveal the drug-likeness properties and binding potentials of both model ($D_2$-$A_2$-$D_2$) [41–43] and newly designed ($D_n$-$A_n$-$D_n$) organic luminogens (Figure 1) with blood proteins, namely bovine serum albumin (BSA) and human serum albumin (HSA), which have emerged as a carrier for a variety of anticancer and anti-infectious drug molecules.
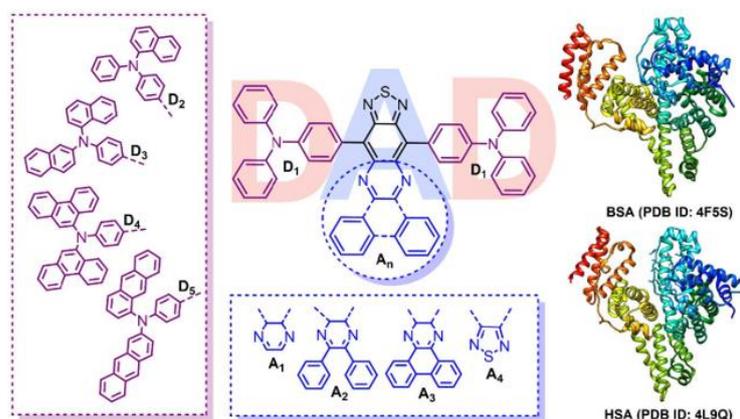


**Figure 1.** Scope of the investigated organic luminogens and target serum albumins (HSA and BSA)

For each docking procedure involving BSA and HSA, the conformation with the highest binding score was chosen. Their binding poses, residue interactions, and docking scores were shown in the relevant parts of the manuscript. These results provide valuable insights into the specific binding interactions between the proteins and the ligands, shedding light on their potential therapeutic

applications. Detailed information about the remaining ligands and macromolecule complexes was provided in the Electronic Supplementary Information (ESI†).

## MATERIAL AND METHOD

### Density Functional Theory (DFT) Calculations

The Gaussian 09 package was used to analyze several quantum chemical properties of our investigated luminogens. Accordingly, the target molecules were initially modeled and constructed using GaussView (v. 5.0.8) software, and their initial geometries were predicted with a potential energy surface (PES) scan utilizing the PM6 method. Then, the corresponding geometry optimization calculations were done using Density Functional Theory (DFT) at the B3LYP level of theory and the 6-31G(d,p) basis set. The DFT calculations were carried out to obtain accurate electronic structures and molecular properties of the luminogens. Additionally, the B3LYP functional was selected as it has been widely used for studying organic molecules and has shown good performance in predicting their properties, and the 6-31G(d,p) basis set was chosen to ensure a good balance between computational cost and accuracy.

### In Silico (ADMET/Drug-likeness) Analyses

Lipinski's rule is a crucial guideline used to determine the potential drugability of a compound. It considers various essential factors such as blood-brain barrier permeability (BBB), gastrointestinal absorption (GI), the number of hydrogen bond acceptors (HBA) and hydrogen bond donors (HBD), as well as the compound's lipophilicity measured by the logPo/w partition coefficient between n-octanol and water.

The optimal BBB permeability and GI absorption depend on the compound's molecular weight (MW). The MW should be below or equal to 500 g/mol for adequate oral bioavailability. The values of HBA and HBD significantly impact the compound's ability to bind to macromolecules. Recommended thresholds for HBA and HBD are 10 and 5, respectively. Several mathematical models, such as iLOGP, XLOGP3, WLOGP, MLOGP, and SILICOS-IT, can be employed to assess the lipophilicity of potential drug candidates. The Consensus logPo/w, obtained by averaging the predictions from these five models, offers a robust indicator, with values ideally below 5 [44,45]. When considering the drug-likeness of a potential compound, various descriptive parameters come into play, including the number of rotatable bonds (nROTB), topological polar surface area (TPSA), solubility, and saturation. The nROTB, which significantly influences the molecule's flexibility, should be kept below 9 for optimal drug-like characteristics.

Moreover, the topological polar surface area (TPSA) represents an additional parameter exclusively based on the fragmental system developed by Ertl et al. Its incorporation has proven instrumental as a descriptor in various models and rules, facilitating the quick estimation of ADME properties. Notably, TPSA exhibits particular relevance in predicting the crossing of compounds through biological barriers, especially in absorption and brain permeability. The recommended TPSA value typically varies from 20 to 130Å$^2$.

Additionally, a soluble compound offers numerous advantages in drug development, primarily ease of handling and formulation. Notably, for drugs intended for parenteral administration, high water solubility is essential to ensure the effective delivery of an adequate amount of the active ingredient within the limited volume of the pharmaceutical dosage. The decimal logarithm of the molar solubility in water (logS) is employed to calculate predicted values, whose optimal logS value should be less than 6. Furthermore, saturation is a vital factor that influences the physicochemical characteristics of a potential drug molecule. It quantifies the ratio of sp$^3$ hybridized carbons to the total carbon count in the molecule. It is advised that the estimated saturation value should be no less than 0.25 [46,47].

In this scope, the SwissADME web tool was employed to assess the drug-likeness and pharmacological behavior of the prospective drug molecules. Additionally, bioavailability radar representations were generated to visually represent molecular descriptors such as lipophilicity (XLOGP3), size (MW), polarity (TPSA), solubility (logS), saturation, and flexibility (nROTB). Furthermore, these properties were also calculated and validated along with the additional analysis of

bioactivity parameters using Molinspiration. OSIRIS Property Explorer (v.4.5.1) revealed several toxicity parameters, including mutagenicity, tumorigenicity, irritation, and reproductive effect.

## Molecular Docking Studies

The 2D structures of the ligands were obtained using ChemDraw. As indicated, the ligands were minimized and optimized using Gaussian 09 software (B3LYP/6-31G(d,p); refer to ESI† for further details) before initiating the molecular docking simulations.

Molecular docking analyses were performed on the dye-albumin complexes SAMSON 2022 R2 modeling platform and Autodock-vina extension. The resulting docking interactions were visualized using Discovery Studio Visualizer 2021 (client version; Accelrys Software Inc., San Diego, CA, USA). The X-ray crystal structures of Bovine Serum Albumin (BSA, PDB ID: 4F5S) and Human Serum Albumin (HSA, PDB ID: 4L9Q) were obtained from the Protein Data Bank (www.rcsb.org). Preprocessing steps were carried out, including the removal of water molecules and any existing ligands' addition of charges and hydrogens to the structures of HSA and BSA for docking purposes. Chain B of both HSA and BSA structures was eliminated, and Chain A was selected for the subsequent molecular docking process. The grid box size was set at 75.7 x 73.2 x 113.8 Å³ with a grid point spacing of 0.375 Å, and the center coordinates of the grid box were defined as x = 2.2, y = -1.6, and z = 28.2.

## RESULT AND DISCUSSION

### Prediction of Drug-likeness and Pharmacokinetic

SwissADME was employed to predict pharmacological properties to investigate the druggability of our tested ligands initially. In this scope, molecular weight (MW), hydrogen bond acceptor (HBA), hydrogen bond donor (HBD), consensus logP ($CLogP_{o/w}$), number of rotatable bonds (nROTBs), topological polar surface area (TPSA), gastrointestinal absorption (GI abs.), blood-brain barrier (BBB), and solubility (S) were determined and listed in Table 1.

**Table 1.** ADME prediction of the investigated dye molecules

| Ligands | MW[a] | HBA[b] | HBD[c] | nROTB[d] | TPSA[e] | GI abs.[f] | BBB[g] | CLog P$_{o/w}$[h] | S[i] |
|---|---|---|---|---|---|---|---|---|---|
| Model Dye | 927 | 4 | 0 | 10 | 86.28 | L | No | 12.96 | Ins |
| D$_1$-A$_1$-D$_1$ | 675 | 4 | 0 | 8 | 86.28 | L | No | 8.72 | Ins |
| D$_1$-A$_2$-D$_1$ | 827 | 4 | 0 | 10 | 86.28 | L | No | 11.25 | Ins |
| D$_1$-A$_3$-D$_1$ | 825 | 4 | 0 | 8 | 86.28 | L | No | 11.53 | Ins |
| D$_1$-A$_4$-D$_1$ | 681 | 4 | 0 | 8 | 114.52 | L | No | 6.9 | Ins |
| D$_2$-A$_1$-D$_2$ | 775 | 4 | 0 | 8 | 86.28 | L | No | 10.46 | Ins |
| D$_2$-A$_3$-D$_2$ | 925 | 4 | 0 | 8 | 86.28 | L | No | 13.19 | Ins |
| D$_2$-A$_4$-D$_2$ | 781 | 4 | 0 | 8 | 114.52 | L | No | 8.46 | Ins |
| D$_3$-A$_1$-D$_3$ | 875 | 4 | 0 | 8 | 86.28 | L | No | 12.18 | Ins |
| D$_3$-A$_2$-D$_3$ | 1027 | 4 | 0 | 10 | 86.28 | L | No | 14.66 | Ins |
| D$_3$-A$_3$-D$_3$ | 1025 | 4 | 0 | 8 | 86.28 | L | No | 14.85 | Ins |
| D$_3$-A$_4$-D$_3$ | 881 | 4 | 0 | 8 | 114.52 | L | No | 10 | Ins |
| D$_4$-A$_1$-D$_4$ | 1075 | 4 | 0 | 8 | 86.28 | L | No | 15.38 | Ins |
| D$_4$-A$_2$-D$_4$ | 1228 | 4 | 0 | 10 | 86.28 | L | No | 17.76 | Ins |
| D$_4$-A$_3$-D$_4$ | 1226 | 4 | 0 | 8 | 86.28 | L | No | 18.16 | Ins |
| D$_4$-A$_4$-D$_4$ | 1081 | 4 | 0 | 8 | 114.52 | L | No | 13.05 | Ins |
| D$_5$-A$_1$-D$_5$ | 1075 | 4 | 0 | 8 | 86.28 | L | No | 15.41 | Ins |
| D$_5$-A$_2$-D$_5$ | 1228 | 4 | 0 | 10 | 86.28 | L | No | 17.88 | Ins |
| D$_5$-A$_3$-D$_5$ | 1226 | 4 | 0 | 8 | 86.28 | L | No | 18.08 | Ins |
| D$_5$-A$_4$-D$_5$ | 1081 | 4 | 0 | 8 | 114.52 | L | No | 13 | Ins |

Rules: [a]MW≤500 g/mol, [b]HBA≤5, [c]HBD≤10, [d]nROTB≤9, 20≤[e]TPSA≤130Å², [h]CLogP$_{o/w}$≤5

Abbreviations: [f]GI abs: Gastrointestinal absorption, [g]BBB: Blood-brain barrier, CLogP$_{o/w}$: Consensus logP$_{o/w}$ [i]S: Solubility
L: Low, Ins: Insoluble

According to the results, the size of our ligands has crossed the threshold (MW≤500 g/mol), and it is deduced that none of the molecules meet the criteria to cross the blood-brain barrier (BBB) and gastrointestinal absorption (GI abs.) for these ligands could not be possible. Another key chemical factor for determining the oral bioavailability of small compounds is the amount of hydrogen bond acceptors (HBA) and donors (HBD). These standards are believed to affect passive diffusion across cell membranes, a critical process during medication absorption and distribution [48].

Our results showed that 4 hydrogen bond acceptors were present in the entire set of our ligands; however, no HBDs were detected. These numbers fell within the intended range and satisfied the criterion. Moreover, the consensus $logP_{o/w}$ parameter, denoting the partition coefficient between n-octanol and water, is a pivotal descriptor employed to evaluate the lipophilicity of a drug molecule. It serves as a crucial criterion in adherence to Lipinski's rule, which stipulates that the $logP_{o/w}$ value of a candidate drug should ideally fall below 5. This requirement ensures optimal lipophilicity for efficient transmembrane permeation, as higher lipophilicities may impede cellular uptake.

The consensus $logP_{(o/w)}$ parameter also represents the average value derived from the five models discussed above: iLOGP, XLOGP3, WLOGP, MLOGP, and SILICOS-IT. These models are utilized to evaluate the lipophilicity of a drug molecule, providing a comprehensive assessment from multiple perspectives. The findings from Table 1 revealed a consistent pattern among the analyzed prospective pharmaceuticals, as they all exhibited lipophilic characteristics that exceeded the desired target range. Specifically, $D_4$-$A_1$-$D_4$ stands out with a relatively lower $ClogP_{o/w}$ value of 6.9 compared to model dye and other ligands, which exhibited a significantly higher value of 12.96. As a consequence of their extreme lipophilicity, all of these compounds were determined to be water-insoluble. The number of rotatable bonds (nROTBs) serves as a significant parameter to assess the flexibility of a drug molecule and its ability to bind to macromolecules. Potent drugs are expected to possess an appropriate number of rotatable bonds (nROTBs) within the upper limit of 9, ensuring sufficient flexibility for effective binding to target macromolecules. Table 1 shows that $D_1$-$A_2$-$D_1$, $D_3$-$A_2$-$D_3$, $D_4$-$A_2$-$D_4$, and $D_5$-$A_2$-$D_5$ exceeded the upper limit of the nROTBs. Notably, these compounds belong to a series of candidate drug molecules composed of various donor and acceptor fragments. Upon closer analysis, it becomes apparent that the excessive number of rotatable bonds is primarily attributed to the $A_2$ unit, which comprises a 5,6-diphenyl-2,3-dihydropyrazine backbone. This acceptor fragment consists of two rotatable phenyl rings bonded to a dihydropyrazine ring.

Consequently, the prospective photosensitizers containing the $A_2$ fragment exhibit two additional nROTBs, resulting in a total of 10 and surpassing the upper limit. In contrast, the remaining ligands in the series possess 8 nROTBs, which fall within the desired limit. It is noteworthy that model dye exceeded the optimal limit for nROTBs. Furthermore, polar surface area (PSA) has also emerged as a widely utilized molecular descriptor in the investigation of drug transport via GI absorption and BBB permeation. It represents the cumulative contribution of polar atoms, including oxygen (O), nitrogen (N), and their associated hydrogen atoms, to the molecular surface area, typically in terms of van der Waals interactions. To address the challenge of complex PSA calculations and enable rapid virtual bioavailability screening of large compound libraries, Ertl et al. developed an efficient additive fragment-based method for PSA computation. The predicted optimal value for TPSA is generally considered to be less than 130 Å². Analyzing the TPSA data presented in Table 1, it is evident that all of the computed ligands fall within the desired range, indicating that the polarity of our prospective drug molecules is adequate. It is worth noting that the ligands containing the 1,2,5-thiadiazole acceptor scaffold (A4) exhibit a higher TPSA value of 114.52 Å², while the TPSA values of the other ligands are 86.28 Å². This disparity can be attributed to the presence of two nitrogen atoms and one sulfur atom in the thiadiazole unit, contributing to increased polarity and, consequently, a higher TPSA value.

Bioavailability radars serve as valuable tools for visualizing the calculated physicochemical data of candidate drug molecules within the context of oral drug-like property space, providing insights into their potential oral bioavailability. In Figure 2, radar plots showcasing the studied molecules with the highest binding affinities to BSA and HSA are depicted, along with model dye. The radar representations of the other investigated luminogens could be accessed in the supplementary material (ESI). The examined parameters, such as lipophilicity, size, solubility, and saturation, as presented in the radar plots, exhibited significant deviations from the hexagonal pink area. However, as expected, the polarity

of our series, as determined by TPSA values, fell within the optimal range. Similarly, the ligands demonstrated optimal flexibility, as derived from nROTBs, except for those containing the 5,6-diphenyl-2,3-dihydropyrazine acceptor unit ($A_2$), surpassing the previously discussed nROTB limit.
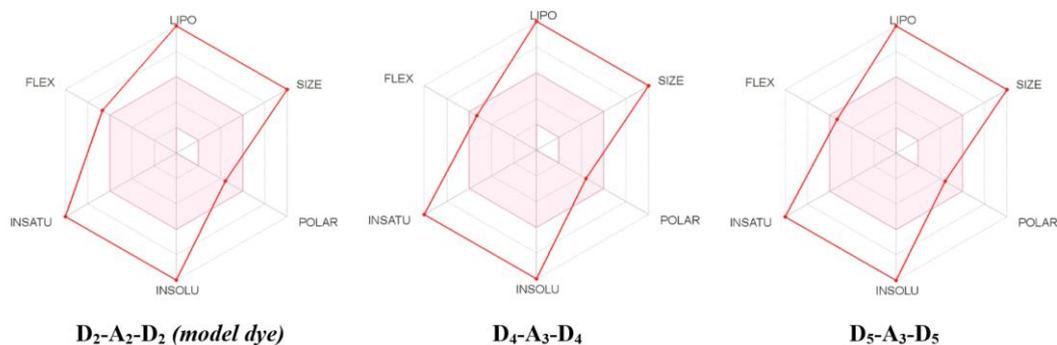


**Figure 2.** Bioavailability radar plots of the studied ligands

To validate the drug-likeness findings obtained from SwissADME, we utilized the Molinspiration Property Calculation tool. Table 2 presents the results of this analysis, specifically the miLogP parameter, which offers a mathematical approach to determine the lipophilicity of potent pharmaceuticals. The computed miLogP values for our ligands ($D_n$-$A_n$-$D_n$) fell within the range of $9.65 < (D_n$-$A_n$-$D_n) < 10.88$, indicating a high level of lipophilicity for our investigated photosensitizers. It is noteworthy that while the miLogP value for our model dye was found to be 10.39, $D_1$-$A_1$-$D_1$ and $D_1$-$A_4$-$D_1$ exhibited relatively lower miLogP values of 9.65 and 9.75, respectively, positioning them closer to the desired range in comparison to the model dye.

**Table 2.** Drug-likeness data for the candidate drug molecules

| Ligands | miLogP[a] | TPSA[b] | nAtoms[c] | nON[d] (HBA) | nOHNH[e] (HBD) | Violation | nROTB[f] | Volume |
|---|---|---|---|---|---|---|---|---|
| **Model Dye** | 10.39 | 58.04 | 71 | 6 | 0 | 2 | 10 | 830.93 |
| **$D_1$-$A_1$-$D_1$** | 9.65 | 58.04 | 51 | 6 | 0 | 2 | 8 | 600.13 |
| **$D_1$-$A_2$-$D_1$** | 10.15 | 58.04 | 63 | 6 | 0 | 2 | 10 | 742.95 |
| **$D_1$-$A_3$-$D_1$** | 10.2 | 58.04 | 63 | 6 | 0 | 2 | 8 | 732.11 |
| **$D_1$-$A_4$-$D_1$** | 9.75 | 56.99 | 50 | 6 | 0 | 2 | 8 | 590.84 |
| **$D_2$-$A_1$-$D_2$** | 10.02 | 58.04 | 59 | 6 | 0 | 2 | 8 | 688.12 |
| **$D_2$-$A_3$-$D_2$** | 10.43 | 58.04 | 71 | 6 | 0 | 2 | 8 | 820.09 |
| **$D_2$-$A_4$-$D_2$** | 10.09 | 56.99 | 58 | 6 | 0 | 2 | 8 | 678.83 |
| **$D_3$-$A_1$-$D_3$** | 10.29 | 58.04 | 67 | 6 | 0 | 2 | 8 | 776.1 |
| **$D_3$-$A_2$-$D_3$** | 10.58 | 58.04 | 79 | 6 | 0 | 2 | 10 | 918.92 |
| **$D_3$-$A_3$-$D_3$** | 10.62 | 58.04 | 79 | 6 | 0 | 2 | 8 | 908.08 |
| **$D_3$-$A_4$-$D_3$** | 10.35 | 56.99 | 66 | 6 | 0 | 2 | 8 | 766.81 |
| **$D_4$-$A_1$-$D_4$** | 10.67 | 58.04 | 83 | 6 | 0 | 2 | 8 | 952.07 |
| **$D_4$-$A_2$-$D_4$** | 10.88 | 58.04 | 95 | 6 | 0 | 2 | 10 | 1094.88 |
| **$D_4$-$A_3$-$D_4$** | 10.9 | 58.04 | 95 | 6 | 0 | 2 | 8 | 1084.04 |
| **$D_4$-$A_4$-$D_4$** | 10.7 | 56.99 | 82 | 6 | 0 | 2 | 8 | 942.78 |
| **$D_5$-$A_1$-$D_5$** | 10.67 | 58.04 | 83 | 6 | 0 | 2 | 8 | 952.07 |
| **$D_5$-$A_2$-$D_5$** | 10.88 | 58.04 | 95 | 6 | 0 | 2 | 10 | 1094.88 |
| **$D_5$-$A_3$-$D_5$** | 10.9 | 58.04 | 95 | 6 | 0 | 2 | 8 | 1084.04 |
| **$D_5$-$A_4$-$D_5$** | 10.71 | 56.99 | 82 | 6 | 0 | 2 | 8 | 942.78 |

[a]miLogP: Partition coefficient between n-octanol and water ($logP_{o/w}$), [b]TPSA: Topological polar surface area, [c]nAtoms: Number of atoms, [d]nON: Number of hydrogen bond acceptors (HBA), [e]nOHNH: Number of hydrogen bond donors (HBD), [f]nROTB: Number of rotatable bonds

Furthermore, the TPSA values of the potent drugs analyzed and listed in the table indicate that the ligands fall below the upper limit of $\leq 130$ Å$^2$, ranging from 56.99 to 58.04 Å$^2$. As mentioned previously, Molinspiration and SwissADME calculations confirm that the polarity, represented by the TPSA value, is sufficient for our investigated potent drugs. According to the Molinspiration analysis, the ligands demonstrated 6 HBAs and 0 HBDs, which fall within the acceptable ranges for these parameters. The number of rotatable bonds (nROTBs) obtained from the analysis agreed with the results from the SwissADME analysis, providing further evidence of the influence of the $A_2$ acceptor fragment (5,6-diphenyl-2,3-dihydropyrazine) on the number of rotatable bonds. Hence, it can be concluded that ligands that do not contain the $A_2$ unit possess an optimal number of rotatable bonds.

**Table 3.** Bioactivity score for the candidate drug molecules

| Ligands | GPCRL[a] | ICM[b] | KI[c] | NRL[d] | PI[e] | EI[f] |
|---|---|---|---|---|---|---|
| Model Dye | -3.63 | -3.78 | -3.74 | -3.77 | -3.57 | -3.7 |
| $D_1$-$A_1$-$D_1$ | -0.73 | -1.75 | -1.26 | -1.38 | -0.53 | -1.16 |
| $D_1$-$A_2$-$D_1$ | -2.94 | -3.61 | -3.51 | -3.56 | -2.48 | -3.32 |
| $D_1$-$A_3$-$D_1$ | -2.96 | -3.59 | -3.51 | -3.57 | -2.49 | -3.29 |
| $D_1$-$A_4$-$D_1$ | -0.64 | -1.62 | -1.23 | -1.23 | -0.47 | -1.08 |
| $D_2$-$A_1$-$D_2$ | -2.11 | -3.27 | -2.91 | -3.06 | -1.62 | -2.68 |
| $D_2$-$A_3$-$D_2$ | -3.63 | -3.77 | -3.75 | -3.78 | -3.57 | -3.69 |
| $D_2$-$A_4$-$D_2$ | -1.93 | -3.16 | -2.83 | -2.88 | -1.47 | -2.52 |
| $D_3$-$A_1$-$D_3$ | -3.45 | -3.70 | -3.65 | -3.68 | -3.14 | -3.59 |
| $D_3$-$A_2$-$D_3$ | -3.78 | -3.87 | -3.85 | -3.87 | -3.76 | -3.82 |
| $D_3$-$A_3$-$D_3$ | -3.79 | -3.87 | -3.85 | -3.88 | -3.76 | -3.81 |
| $D_3$-$A_4$-$D_3$ | -3.36 | -3.68 | -3.65 | -3.66 | -3.01 | -3.57 |
| $D_4$-$A_1$-$D_4$ | -3.83 | -3.90 | -3.89 | -3.9 | -3.81 | -3.86 |
| $D_4$-$A_2$-$D_4$ | -3.93 | -3.98 | -3.97 | -3.98 | -3.92 | -3.95 |
| $D_4$-$A_3$-$D_4$ | -3.93 | -3.97 | -3.97 | -3.99 | -3.92 | -3.94 |
| $D_4$-$A_4$-$D_4$ | -3.83 | -3.90 | -3.89 | -3.9 | -3.80 | -3.86 |
| $D_5$-$A_1$-$D_5$ | -3.83 | -3.90 | -3.89 | -3.91 | -3.8 | -3.86 |
| $D_5$-$A_2$-$D_5$ | -3.93 | -3.98 | -3.97 | -3.98 | -3.92 | -3.95 |
| $D_5$-$A_3$-$D_5$ | -3.93 | -3.98 | -3.97 | -3.99 | -3.92 | -3.94 |
| $D_5$-$A_4$-$D_5$ | -3.83 | -3.90 | -3.90 | -3.90 | -3.79 | -3.86 |

[a]GPCRL: G protein-coupled receptor ligands Ligands, [b]ICM: Ion Channel Modulator, [c]KI: Kinase Inhibitor, [d]NRL: Nuclear Receptor Ligand, [e]PI: Protease Inhibitor, [f]EI: Enzyme Inhibitor

The utilization of the Molinspiration platform enables the calculation of diverse bioactivity descriptors. These descriptors include GPCR Ligands (GPCRL), Ion Channel Modulator (ICM), Nuclear Receptor Ligand (NRL), Protease Inhibitor (PI), and Enzyme Inhibitor (EI). For a compound to be designated as a potential drug, it is imperative for it to exhibit a bioactivity score surpassing 0.0, denoting a significant level of bioactivity. Conversely, bioactivity scores ranging from -0.50 to 0.0 indicate moderate activity, whereas below -0.50 indicates a lack of bioactivity [49]. GPCR ligands, specifically G protein-coupled receptor ligands, are integral members of a diverse family of signaling proteins responsible for cellular responses to hormones, metabolites, cytokines, and neurotransmitters. Their exceptional druggability and pivotal role in major diseases render them highly attractive drug discovery and development targets. In parallel, ion channels are the foundation for numerous physiological processes, including rapid cell reconfigurations, cardiac and muscular contractions, neuronal activity, and tumor cell proliferation.

Various chemical compounds such as antibodies, peptides, small molecules, or ions function as ion-channel modulators through interactions with membrane proteins, exerting a crucial influence on ion-channel function [50]. The kinase family has been widely researched as a therapeutic target for 30 years. In addition to metastatic cancer, the deregulation of kinase activity has been demonstrated to

contribute to immune, inflammatory, degenerative, metabolic, cardiovascular, and viral diseases. Due to their proven druggability and the clinical safety profile of approved kinase inhibitors, kinases are attractive targets for small molecules [51]. Nuclear Receptors (NRs) are ligand-induced transcription factors that translocate to the nucleus and directly control gene transcription. They play a crucial role in vital physiological processes such as cell growth, development, immunity, metabolism, and reproduction of cancer cells [52]. Table 3 presents the outcomes of the calculated parameters for our investigated ligands, indicating that none met the criteria to be classified as bioactive compounds. Specifically, upon evaluating the GPCRL scores, it is evident that $D_1$-$A_1$-$D_1$ and $D_1$-$A_4$-$D_1$ ligands possessed moderate bioactivity with -0.73 and -0.64, respectively. The remaining part of our models exhibited inactivity, ranging from -3.93 to -0.64.

Similarly, none of our ligands displayed bioactivity for Ion Channel Modulator (ICM) scores, ranging from -3.98 to -1.62. Kinase Inhibitor (KI) scores further revealed that our potent drugs exhibited values below the optimal bioactivity threshold, ranging from -3.97 to -1.26. Furthermore, the analysis of Nuclear Receptor Ligand (NRL) characteristics indicated that our ligands fell below the desired limit. Likewise, the scores for Protease Inhibitors (PIs) and Enzyme Inhibitors (EIs), which play significant roles in physiological processes, demonstrated that the majority of our ligands did not meet the criteria to be considered bioactive compounds. However, it is noteworthy to mention that $D_1$-$A_4$-$D_1$ and $D_1$-$A_1$-$D_1$ exhibited moderate protease inhibitory activity, with scores of -0.47 and -0.53, respectively. These findings highlight the potential of these compounds for the treatment of certain cancers associated with protease enzymes. Based on these results, it is essential to pursue various lead optimization strategies to achieve bioactivity within the desired range.

The toxicity risk factors of the luminogens, such as mutagenicity, tumorigenicity, skin irritability, and reproductive consequences, were evaluated using OSIRIS software. To support the previous findings, solubility and lipophilicity were also determined. Additionally, the studied photosensitizers' drug-likeness and drug scores were assessed to further assess the druggability of the compounds. The results are illustrated in Table 4.

**Table 4.** Druglikeness and toxicity risk data of the investigated ligands

| Ligands | cLogp | Solubility | Druglikeness | Drug Score | Mutagenic | Tumorigenic | Irritant | Reproductive Effective |
|---|---|---|---|---|---|---|---|---|
| Model Dye | 16.01 | -17.35 | 0.36 | 0.04 | 🔴 | 🔴 | 🟢 | 🟢 |
| $D_1$-$A_1$-$D_1$ | 10.12 | -10.58 | -0.27 | 0.06 | 🔴 | 🟢 | 🟢 | 🟢 |
| $D_1$-$A_2$-$D_1$ | 13.62 | -14.13 | -2.84 | 0.04 | 🔴 | 🟢 | 🟢 | 🟢 |
| $D_1$-$A_3$-$D_1$ | 13.95 | -15.19 | -4.63 | 0.04 | 🔴 | 🟢 | 🟢 | 🟢 |
| $D_1$-$A_4$-$D_1$ | 11.20 | -7.40 | -0.67 | 0.06 | 🔴 | 🟢 | 🟢 | 🟢 |
| $D_2$-$A_1$-$D_2$ | 12.51 | -13.79 | 2.94 | 0.05 | 🔴 | 🔴 | 🟢 | 🟢 |
| $D_2$-$A_3$-$D_2$ | 16.34 | -18.4 | -1.38 | 0.03 | 🔴 | 🔴 | 🟢 | 🟢 |
| $D_2$-$A_4$-$D_2$ | 13.59 | -10.62 | 2.55 | 0.04 | 🔴 | 🔴 | 🟢 | 🟢 |
| $D_3$-$A_1$-$D_3$ | 14.90 | -17.00 | -0.07 | 0.03 | 🔴 | 🔴 | 🟡 | 🟢 |
| $D_3$-$A_2$-$D_3$ | 18.40 | -20.56 | -2.64 | 0.02 | 🔴 | 🔴 | 🟡 | 🟢 |
| $D_3$-$A_3$-$D_3$ | 18.73 | -21.6 | -4.42 | 0.02 | 🔴 | 🔴 | 🟡 | 🟢 |
| $D_3$-$A_4$-$D_3$ | 15.98 | -13.83 | -0.49 | 0.03 | 🔴 | 🔴 | 🟡 | 🟢 |
| $D_4$-$A_1$-$D_4$ | 19.68 | -23.43 | 2.48 | 0.03 | 🔴 | 🔴 | 🟡 | 🟢 |
| $D_4$-$A_2$-$D_4$ | 23.18 | -26.93 | -0.10 | 0.03 | 🔴 | 🔴 | 🟡 | 🟢 |
| $D_4$-$A_3$-$D_4$ | 23.50 | -28.03 | -1.92 | 0.02 | 🔴 | 🔴 | 🟡 | 🟢 |
| $D_4$-$A_4$-$D_4$ | 20.76 | -20.25 | 2.05 | 0.03 | 🔴 | 🔴 | 🟡 | 🟢 |
| $D_5$-$A_1$-$D_5$ | 19.68 | -23.43 | -1.64 | 0.02 | 🔴 | 🔴 | 🔴 | 🟢 |
| $D_5$-$A_2$-$D_5$ | 23.18 | -26.93 | -4.23 | 0.01 | 🔴 | 🔴 | 🔴 | 🟢 |
| $D_5$-$A_3$-$D_5$ | 23.50 | -28.03 | -6.01 | 0.01 | 🔴 | 🔴 | 🔴 | 🟢 |
| $D_5$-$A_4$-$D_5$ | 20.76 | -20.25 | -2.06 | 0.02 | 🔴 | 🔴 | 🔴 | 🟢 |

🔴: High toxicity, 🟡: Moderate toxicity, 🟢: No detectable toxicity

The lipophilicity and solubility results obtained from the SwissADME and Molinspiration analyses were in line with the findings from the OSIRIS analysis. Notably, these two parameters provide complementary information, as lipophilicity and water solubility are inversely proportional to each other. Consistent with expectations, the OSIRIS analysis indicated that our luminogens exhibited considerably high lipophilicity, ranging from 10.12 to 23.50. In contrast, the water solubility of the ligands varied between -28.03 and -7.40. Consequently, to comprehend the pharmacological properties of our ligands, drug-likeness and drug score factors were analyzed [53]. Equation 1 calculates the drug-likeness (d), where $V_i$ indicates scores of molecular fragments and n denotes the number of molecular fragments.

$$d = \frac{\sum V_i}{\sqrt{n}}$$                                                                Equation 1

Equation 2 is used to obtain the drug score (ds) of the examined sensitizers, where the $s_i$ parameter represents the contributions calculated directly from cLogP, logS, molecular weight, and drug-likeness, and $t_i$ represents the contribution taken from the four toxicity risk classes.

$$ds = \pi\left(\frac{1}{2} + \frac{1}{2}si\right).\pi ti$$                                     Equation 2

The data showed that $D_2$-$A_n$-$D_2$ and $D_4$-$A_n$-$D_4$ series (including model dye, denoted as $D_2$-$A_2$-$D_2$) have better drug-likeness (d) potential. More specifically, $D_2$-$A_1$-$D_2$ and D2-A4-D2 have 2.94 and 2.55 drug-likeness values, respectively, and $D_4$-$A_1$-$D_4$ and $D_4$-$A_4$-$D_4$ possess 2.48 and 2.05 drug-likeness values, respectively. These scores are found to be much higher in comparison with model dye possessing a 0.36 drug-likeness value. Subsequently, considering the drug scores, the $D_1$-$A_n$-$D_1$ series have been determined to be more prominent than other series. Specifically, $D_1$-$A_1$-$D_1$ and $D_1$-$A_4$-$D_1$ have the same drug score (ds) of 0.06, and in the case of $D_2$-$A_1$-$D_2$, this value was found to be 0.05, three of which ligands have higher drug scores when compared to model dye having 0.04 ds value. In addition, the assessment of potential toxicity risk parameters, as presented in Table 4, has provided valuable insights. Our findings indicate that the studied ligands exhibit a high level of mutagenicity, raising concerns about their potential to induce genetic mutations.

Additionally, all investigated ligands, except for the $D_1$-$A_n$-$D_1$ series, display a high tumorigenicity profile. These characteristics are highly undesirable in drug molecules as they can contribute to cancer development by promoting the malignant proliferation of cells. Furthermore, evaluating irritancy, skin irritation, and reproductive effectiveness parameters is crucial in assessing the potential toxic effects of compounds. Ligands with irritancy properties can harm human skin, leading to reactions such as burning sensations, stinging, and redness. Our analysis reveals that the $D_1$-$A_n$-$D_1$ and $D_2$-$A_n$-$D_2$ ligands do not exhibit skin irritation characteristics, while the $D_3$-$A_n$-$D_3$ and $D_4$-$A_n$-$D_4$ series display a moderate irritancy property. Notably, the $D_5$-$A_n$-$D_5$ series of ligands demonstrate a considerably high level of irritation, which is undesirable in a drug molecule. Moreover, assessing reproductive effects is important in determining whether a candidate drug molecule impacts the reproductive system of the human body. According to the data obtained from OSIRIS, none of the investigated photosensitizers exhibit any reproductive effects.

## Molecular Docking Study

Molecular docking is a popular computational strategy for drug development that enables the evaluation of the potential for interaction between ligands and macromolecules like proteins. It allows for detecting new pharmaceuticals and the molecular-level prediction of interactions between ligands and their target molecules. Furthermore, docking facilitates the exploration of structure-activity correlations (SAR) without prior knowledge of the chemical structure of the target modulators. While initially developed to study the molecular recognition mechanisms between small and large molecules, the application of docking in drug development has evolved significantly in recent years.

The primary objective of this study is to evaluate the binding capabilities of newly designed luminogens, specifically the $D_n$-$A_n$-$D_n$ series, with albumin proteins, including bovine serum albumin (BSA) and human serum albumin (HSA). These albumin proteins have emerged as robust carriers for

various pharmaceuticals in treating cancer and infectious diseases. Therefore, a comprehensive molecular docking strategy has been employed. Initially, a series of well-known NIR-I and NIR-II AIEgens were investigated, serving as model dyes commonly used in photodynamic therapy (PDT). Subsequently, modifications were made to these model dyes' acceptor and donor units to enhance their selectivity and binding affinities with BSA (PDB ID: 4F5S) and HSA (PDB ID: 4L9Q). These albumin proteins have shown to be effective pharmacological carriers for various drugs used to treat cancer and infectious disorders. The investigation began with several NIR-I and NIR-II AIEgens, a widely known luminogen family frequently employed in photodynamic treatment (PDT). These model dyes' acceptor and donor units were then altered to improve their selectivity and binding affinities with BSA (PDB ID: 4F5S) and HSA (PDB ID: 4L9Q).

The molecular docking simulations were performed for 20 newly designed photosensitizers, and the resulting binding scores and binding domains are presented in Table 5. Detailed information regarding the residue category, type of interactions, residue distance from the binding domain, and specific residue information can be found in the electronic supplementary information (ESI†). This comprehensive approach provides insights into the binding affinities and interactions between the investigated ligands and albumin proteins, contributing to our understanding of their potential as therapeutic agents. BSA and HSA are well-known for their distinct structural compositions, consisting of three main domains (Domain I, Domain II, and Domain III), which comprise two subdomains each (IA, IB, IIA, IIB, IIIA, and IIIB).

Crystal structural investigations have revealed that the primary ligand binding sites in BSA and HSA are located in hydrophobic voids within subdomains IIA and IIIA, known as Sudlow's site I and Sudlow's site II, respectively. Table 5 demonstrates the binding interactions between our investigated organic luminogens and the ligand-binding subdomains. Interestingly, the $D_1$-$A_n$-$D_1$ series exhibited interactions with different subdomains compared to the other studied luminogens. Specifically, $D_1$-$A_1$-$D_1$ bonded to the IIIB subdomain, while $D_1$-$A_2$-$D_1$ and $D_1$-$A_3$-$D_1$ interacted with IB, IIA, and IIIA subdomains. $D_1$-$A_4$-$D_1$ targeted both IIIA and IIIB subdomains. The remaining series of luminogens, including $D_2$-$A_n$-$D_2$, $D_3$-$A_n$-$D_3$, $D_4$-$A_n$-$D_4$, and $D_5$-$A_n$-$D_5$, selected IA and IB subdomains as their binding sites. Furthermore, the binding interactions between the ligands and HSA were more complex than the ligand-BSA complexes. The majority of the ligands were in co-interaction with IB, IIA, and IIIA subdomains. This binding interaction was observed in $D_1$-$A_3$-$D_1$, $D_2$-$A_3$-$D_2$, $D_3$-$A_{(1,2,3)}$-$D_3$, $D_4$-$A_n$-$D_4$ and $D_5$-$A_{(2,3)}$-$D_5$. In addition, several ligands, including $D_2$-$A_4$-$D_2$, $D_3$-$A_4$-$D_3$, $D_5$-$A_1$-$D_5$, and $D_5$-$A_4$-$D_5$, selected IA and IB sub-domains as binding targets. The remaining luminogens selected different binding sites other than the rest of the ligands. Specifically, $D_1$-$A_1$-$D_1$ & IA, $D_1$-$A_2$-$D_1$ & IIB and IIA, $D_1$-$A_4$-$D_1$ & IIA, and IIIA and $D_2$-$A_1$-$D_2$ & IB binding interactions were observed. It is noteworthy that model dye is bound to IA and IB sub-domains of the BSA and IB, IIA, and IIIA sub-domains of the HSA.

Most ligands exhibited binding interactions with IB, IIA, and IIIA subdomains. This pattern was observed in ligands such as $D_1$-$A_3$-$D_1$, $D_2$-$A_3$-$D_2$, $D_3$-$A_{(1,2,3)}$-$D_3$, $D_4$-$A_n$-$D_4$, and $D_5$-$A_{(2,3)}$-$D_5$. Conversely, other ligands, including $D_2$-$A_4$-$D_2$, $D_3$-$A_4$-$D_3$, $D_5$-$A_1$-$D_5$, and $D_5$-$A_4$-$D_5$, targeted IA and IB subdomains as their binding sites. The remaining luminogens displayed unique binding interactions distinct from the rest. For instance, $D_1$-$A_1$-$D_1$ bound to IA subdomain, $D_1$-$A_2$-$D_1$ interacted with IIB and IIA subdomains, $D_1$-$A_4$-$D_1$ targeted IIA and IIIA subdomains, and $D_2$-$A_1$-$D_2$ bound to IB subdomain. It is worth noting that the model dye exhibited binding to IA and IB subdomains of BSA, whereas IB, IIA, and IIIA subdomains of HSA. The binding poses of the ligand-BSA, and ligand-HSA complexes and their 2D/3D residue interaction representations were illustrated in Table 6 and Table 7, respectively. The electronic supplementary information file provides the complementary binding poses and 2D/3D residue interactions (ESI†).

The docking scores of the ligands, as shown in Table 5, provided insights into their binding affinities. The $D_1$-$A_n$-$D_1$ series exhibited binding affinities ranging from -8.5 kcal/mol to -10.3 kcal/mol, indicating relatively weaker binding compared to the other luminogens, including the model dye with a binding affinity of -10.7 kcal/mol. $D_2$-$A_n$-$D_2$ and $D_3$-$A_n$-$D_3$ series displayed relatively higher docking scores, ranging from -10.5 kcal/mol to -12.7 kcal/mol and -11.9 kcal/mol to -13.2 kcal/mol, respectively. $D_4$-$A_n$-$D_4$ and $D_5$-$A_n$-$D_5$ series, excluding $D_5$-$A_2$-$D_5$, exhibited the highest docking scores, with the $D_4$-

$A_n$-$D_4$ series ranging from -13.8 kcal/mol to -15.1 kcal/mol and the $D_5$-$A_n$-$D_5$ series ranging from -12.3 kcal/mol to -14.0 kcal/mol. Notably, the ligand with the highest docking score in the $D_4$-$A_n$-$D_4$ series, $D_4$-$A_3$-$D_4$, contained two $D_4$ donor fragments [N-(phenanthrene-9-yl)-N-phenylphenanthren-9-amine] with an $A_3$ acceptor unit (2,3-dihydrodibenzo[f,h]quinoxaline) fragment bonded to benzothiadiazole (BTD), which is commonly used in various organic NIR-I and NIR-II luminogens (Figure 3). The docking scores of our investigated luminogens interacting with HSA, listed in decreasing order, are as follows: $D_4$-$A_3$-$D_4$ (-15.1) > $D_5$-$A_1$-$D_5$ (-14.0) > $D_4$-$A_1$-$D_4$ (-13.9) = $D_4$-$A_2$-$D_4$ (-14.3) > $D_4$-$A_4$-$D_4$ (-13.8) > $D_5$-$A_4$-$D_5$ (-13.7) > $D_3$-$A_4$-$D_3$ (-13.2) > $D_5$-$A_3$-$D_5$ (-13.2) > $D_3$-$A_1$-$D_3$ (-12.7) > $D_3$-$A_3$-$D_3$ (-12.6) > $D_5$-$A_2$-$D_5$ (-12.3) > $D_3$-$A_2$-$D_3$ (-11.9) > $D_2$-$A_3$-$D_2$ (-11.8) > $D_2$-$A_1$-$D_2$ (-11.3) > model dye $D_2$-$A_2$-$D_2$ (-10.7)) > $D_2$-$A_4$-$D_2$ (-10.5) > $D_1$-$A_2$-$D_1$ (-10.3) > $D_1$-$A_3$-$D_1$ (-9.6) > $D_1$-$A_1$-$D_1$ = $D_1$-$A_4$-$D_1$ (-8.5).

**Table 5.** Docking scores and binding domain data of the studied ligands with BSA and HSA



| Ligands | Binding score | | Binding domain | |
|---|---|---|---|---|
| | BSA | HSA | BSA | HSA |
| **Model Dye** | -10.7 | -11.8 | IA & IB | IB & IIA & IIIA |
| **$D_1$-$A_1$-$D_1$** | -8.5 | -10.0 | IIIB | IA |
| **$D_1$-$A_2$-$D_1$** | -10.3 | -12.6 | IB & IIA & IIIA | IIB & IIIA |
| **$D_1$-$A_3$-$D_1$** | -9.6 | -12.7 | IB & IIA & IIIA | IB & IIA & IIIA |
| **$D_1$-$A_4$-$D_1$** | -8.5 | -10.1 | IIIA & IIIB | IIA & IIIA |
| **$D_2$-$A_1$-$D_2$** | -11.3 | -12.3 | IA & IB | IB |
| **$D_2$-$A_3$-$D_2$** | -11.8 | -12.8 | IA & IB | IB & IIA & IIIA |
| **$D_2$-$A_4$-$D_2$** | -10.5 | -12.3 | IA & IB | IA & IB |
| **$D_3$-$A_1$-$D_3$** | -12.7 | -13.9 | IA & IB | IB & IIA & IIIA |
| **$D_3$-$A_2$-$D_3$** | -11.9 | -13.2 | IA & IB | IB & IIA & IIIA |
| **$D_3$-$A_3$-$D_3$** | -12.6 | -14.3 | IA & IB | IB & IIA & IIIA |
| **$D_3$-$A_4$-$D_3$** | -13.2 | -13.7 | IA & IB | IA & IB |
| **$D_4$-$A_1$-$D_4$** | -13.9 | -12.6 | IA & IB | IB & IIA & IIIA |
| **$D_4$-$A_2$-$D_4$** | -13.9 | -12.9 | IA & IB | IB & IIA & IIIA |
| **$D_4$-$A_3$-$D_4$** | -15.1 | -13.5 | IA & IB | IB & IIA & IIIA |
| **$D_4$-$A_4$-$D_4$** | -13.8 | -13.1 | IA & IB | IB & IIA & IIIA |
| **$D_5$-$A_1$-$D_5$** | -14.0 | -14.4 | IA & IB | IA & IB |
| **$D_5$-$A_2$-$D_5$** | -12.3 | -14.0 | IA & IB | IB & IIA & IIIA |
| **$D_5$-$A_3$-$D_5$** | -13.2 | -15.9 | IA & IB | IB & IIA & IIIA |
| **$D_5$-$A_4$-$D_5$** | -13.7 | -14.7 | IA & IB | IA & IB |

**Model dye (binding score: -10.7 kcal/mol || binding domain: IA & IB)**



**D₄-A₃-D₄ (binding score: -15.1 kcal/mol || binding domain: IA & IB)**
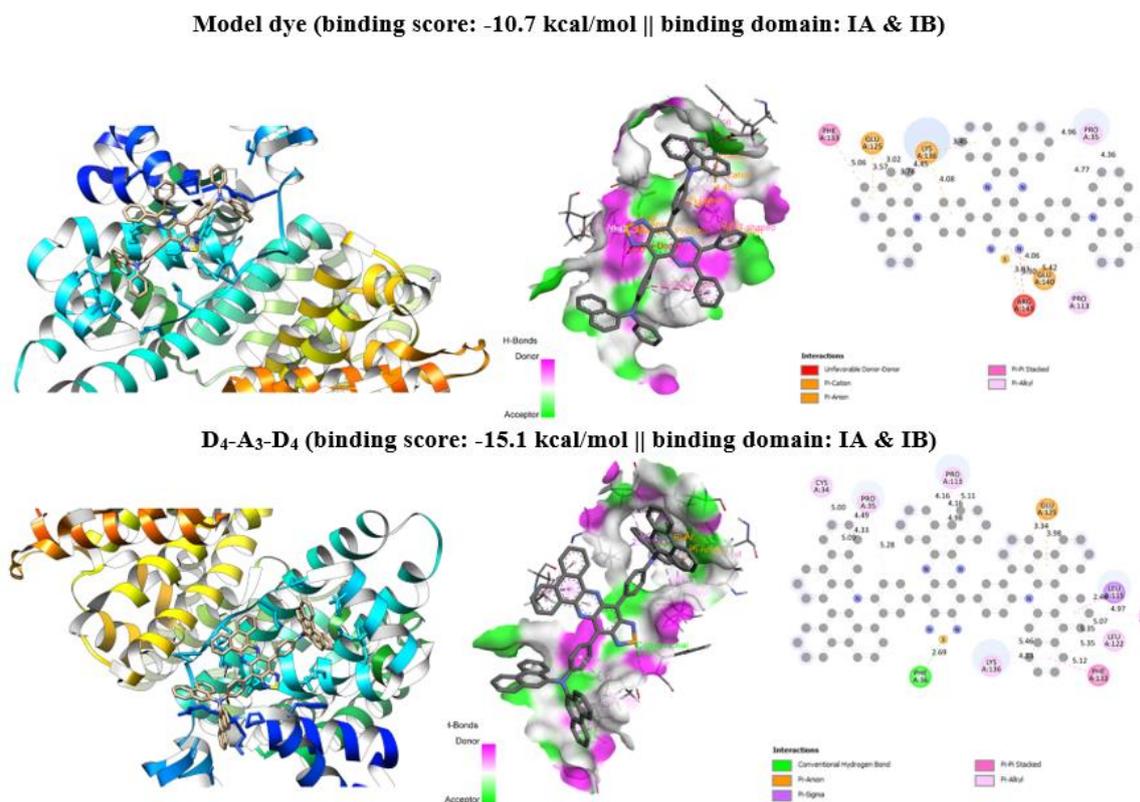


**Figure 3.** Binding poses and residue interactions of the model dye and D₄-A₃-D₄ with BSA

The $D_1$-$A_n$-$D_1$ series exhibited binding affinities ranging from -10 to -12.7 kcal/mol, indicating lower scores than the other ligands. Except for $D_1$-$A_2$-$D_1$ and $D_1$-$A_3$-$D_1$, which displayed docking scores of -12.6 kcal/mol and -12.7 kcal/mol, respectively, the ligands in this series had lower scores than the model dye (-11.8 kcal/mol). Notably, the $D_2$-$A_n$-$D_2$ series demonstrated higher docking scores, ranging from -12.3 to -12.8 kcal/mol. Among the investigated sensitizers, the $D_3$-$A_n$-$D_3$, $D_4$-$A_n$-$D_4$ (excluding $D_4$-$A_1$-$D_4$ with relatively lower scores), and $D_5$-$A_n$-$D_5$ series exhibited the highest docking scores. The docking scores for the $D_3$-$A_n$-$D_3$ series ranged from -13.2 to -14.3 kcal/mol, while those for the D4-An-D4 ligands ranged from -12.6 to -13.5 kcal/mol and for the $D_5$-$A_n$-$D_5$ ligands, the scores ranged from -14.4 to -15.9 kcal/mol. Notably, $D_5$-$A_3$-$D_5$ achieved the highest docking score of -15.9 kcal/mol among all the investigated potential drug molecules (Figure 4). When examining the structure of $D_5$-$A_3$-$D_5$, which displayed the best docking score, it consisted of two $D_5$ donor fragments [N-(anthracene-2-yl)-N-phenylanthracen-1-amine] with an $A_3$ acceptor unit (2,3-dihydrodibenzo[f,h]quinoxaline) fragment bonded to a benzothiadiazole (BTD) backbone. The docking scores of our investigated luminogens interacting with BSA can be ranked in descending order as follows: $D_5$-$A_3$-$D_5$ (-15.9) > $D_5$-$A_4$-$D_5$ (-14.7) > $D_5$-$A_1$-$D_5$ (-14.4) > $D_3$-$A_3$-$D_3$ (-14.3) > $D_5$-$A_2$-$D_5$ (-14.0) > $D_3$-$A_1$-$D_3$ (-13.9) > $D_3$-$A_4$-$D_3$ (-13.7) > $D_4$-$A_3$-$D_4$ (-13.5) > $D_3$-$A_2$-$D_3$ (-13.2) > $D_4$-$A_4$-$D_4$ (-13.1) > $D_4$-$A_2$-$D_4$ (-12.9) > $D_2$-$A_3$-$D_2$ (-12.8) > $D_1$-$A_3$-$D_1$ (-12.7) > $D_4$-$A_1$-$D_4$ = $D_1$-$A_2$-$D_1$ (-12.6) > $D_2$-$A_4$-$D_2$ = $D_2$-$A_1$-$D_2$ (-12.3) > model dye {$D_2$-$A_2$-$D_2$} (-11.8) > $D_1$-$A_4$-$D_1$ (-10.1) > $D_1$-$A_1$-$D_1$ (-10.0).

Generally, there is an increasing trend of binding affinities observed from the $D_1$-$A_n$-$D_1$ to $D_5$-$A_n$-$D_5$ series, with some exceptions. In ligand-HSA complexes, more complex residue interactions were observed. It was found that many ligands interacted electrostatically with ARG218 and hydrophobically with LYS195 amino acid residues. Other prominent interactions involved electrostatic interactions with ARG186, GLU294 and hydrophobic interactions with LYS444, PRO447, and TYR452. Notably, the ligand D5-A3-D5, which exhibited the highest binding affinity, interacted electrostatically with

ARG218, GLU292, GLU294, LYS274, LYS444, and hydrophobically with ALA191 and PRO447 amino acid residues.
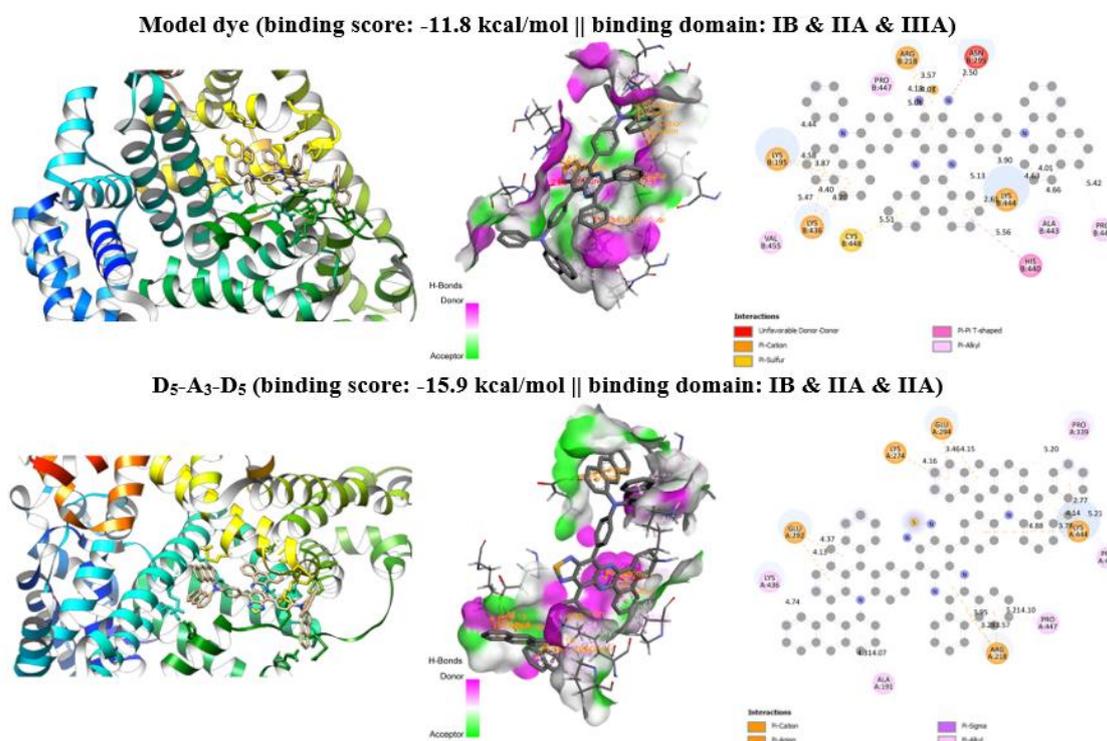


**Figure 4.** Binding poses and residue interactions of the model dye and $D_5$-$A_3$-$D_5$ with HSA

The main objective of this study was to investigate the docking performance of twenty novel organic NIR-I and NIR-II luminogens. Target ligands' drug-likeness and pharmacokinetic properties were assessed with SwissADME, Molinspiration, and OSIRIS to achieve this goal. Molecular docking simulations were also conducted, and the results were analyzed using UCSF-Chimera (v.2021-06-26) and Discovery Studio Visualizer 2021 software. Based on the drug-likeness assessments conducted using SwissADME and Molinspiration, it was found that $D_1$-$A_1$-$D_1$ and $D_1$-$A_4$-$D_1$ exhibited relatively favorable characteristics regarding MW and ClogP$_{o/w}$ values. Specifically, $D_1$-$A_1$-$D_1$ had an MW of 675 g/mol and a ClogP$_{o/w}$ value of 8.72, while $D_1$-$A_4$-$D_1$ had an MW of 681 g/mol and a ClogP$_{o/w}$ value of 6.9.

Furthermore, the Molinspiration study highlighted the lipophilicity (with miLogP approach), and it was observed that $D_1$-$A_1$-$D_1$ and $D_1$-$A_4$-$D_1$ displayed notable miLogP values of 9.65 and 9.75, respectively. These findings indicate that $D_1$-$A_1$-$D_1$ and $D_1$-$A_4$-$D_1$ possessed favorable drug-likeness properties compared to the other investigated luminogens and the model dye. Overall bioactivity scores of our investigated luminogens also showed that $D_1$-$A_1$-$D_1$ and $D_1$-$A_4$-$D_1$ demonstrated moderate bioactivity regarding GPCRL and PI parameters. Moreover, the drug-likeness and drug scores of our luminogens were also validated with OSIRIS. $D_2$-$A_1$-$D_2$ and $D_2$-$A_4$-$D_2$ have a drug-likeness value of 2.94 and 2.55, respectively, whereas $D_4$-$A_1$-$D_4$ and $D_4$-$A_4$-$D_4$ have a value of 2.48 and 2.05, respectively. These values are significantly higher than those for model dye, with a 0.36 score.

Regarding drug scores (ds), the $D_1$-$A_n$-$D_1$ series was more prevalent than the other series. Specifically, $D_1$-$A_1$-$D_1$ and $D_1$-$A_4$-$D_1$ both have a drug score of 0.06, and $D_2$-$A_1$-$D_2$ has a drug score of 0.05, three of which outperformed model dye, which has a 0.04 ds value. In addition, the drug-likeness and drug scores of our luminogens were further comprehended and validated through OSIRIS. Specifically, $D_2$-$A_1$-$D_2$ and $D_2$-$A_4$-$D_2$ demonstrated notable drug-likeness values of 2.94 and 2.55,

respectively, and these values were shifted to 2.48 and 2.04 for $D_4$-$A_1$-$D_4$ and $D_4$-$A_4$-$D_4$, respectively. These values exhibit a significant increase compared to the drug-likeness value of model dye, which stands at a mere 0.36.

Furthermore, regarding drug scores, the D1-An-D1 series displayed a higher prevalence than the other series. Notably, both $D_1$-$A_1$-$D_1$ and $D_1$-$A_4$-$D_1$ achieved a drug score of 0.06, while $D_2$-$A_1$-$D_2$ obtained a slightly lower drug score of 0.05. Remarkably, all three of these ligands surpassed the model dye at 0.04 ds value. OSIRIS analysis further confirmed the consistency of the lipophilicity and water solubility levels of our ligands with the findings from SwissADME and Molinspiration.

Additionally, the assessment of toxicity risks revealed that the entire set of our luminogens exhibited high mutagenic properties. It was also repeated with tumorigenic characteristics, except for the $D_1$-$A_{(1-4)}$-$D_1$ series, which proved safe. Notably, the $D_1$-$A_n$-$D_1$ and $D_2$-$A_n$-$D_2$ series did not exhibit any skin irritation, whereas the $D_3$-$A_n$-$D_3$ and $D_4$-$A_n$-$D_4$ series showed moderate irritancy. On the other hand, the $D_5$-$A_n$-$D_5$ series demonstrated high irritant properties. Furthermore, no reproductive effectiveness was observed in any of the investigated luminogens. Considering all the parameters and properties described, the ligands $D_1$-$A_1$-$D_1$ and $D_1$-$A_4$-$D_1$ appear to be the best druggable ligands. In terms of the binding performances, it was evident that they underperformed model dye, with docking scores of -8.50 g/mol with BSA, and -10.00 and -10.10 g/mol with HSA, respectively. In addition, $D_4$-$A_3$-$D_4$ exhibited the most efficient docking performance with BSA by binding to its IA and IB sub-domains, which showed a -15.1 kcal/mol docking score. On the other hand, $D_5$-$A_3$-$D_5$ bound to IB, IIA, and IIIA sub-domains of HSA demonstrated the best binding affinity as -15.9 kcal/mol. In light of this information, we believe that our prospective NIR dye molecules used in this study will provide a valuable theoretical perspective to research in the field of fluorescence imaging (FLI) based photodynamic cancer therapy (PDT).

## ACKNOWLEDGEMENTS

## AUTHOR CONTRIBUTIONS

Concept: G.K.; Design: H.N., G.K.; Control: G.K.; Sources: G.K.; Materials: H.N., G.K.; Data Collection and/or Processing: H.N., G.K., D.T.Ö., Z.Y.; Analysis and/or Interpretation: H.N., G.K.; Literature Review: H.N., G.K., D.T.Ö., Z.Y.; Manuscript Writing: H.N., G.K.; Critical Review: H.N., G.K., D.T.Ö., Z.Y.; Other: -

## CONFLICT OF INTEREST

The authors declare that there is no real, potential, or perceived conflict of interest for this article.

## ETHICS COMMITTEE APPROVAL

The authors declare that the ethics committee approval is not required for this study.

## REFERENCES

1.  Park, J.W., Han, J.W. (2019). Targeting epigenetics for cancer therapy. Archives of Pharmacal Research, 42(2), 159-170. [CrossRef]
2.  Schuster, E., Taftaf, R., Reduzzi, C., Albert, M.K., Romero-Calvo, I., Liu, H. (2021). Better together: Circulating tumor cell clustering in metastatic cancer. Trends in Cancer, 7(11), 1020-1032. [CrossRef]
3.  Pucci, C., Martinelli, C., Ciofani, G. (2019). Innovative approaches for cancer treatment: Current perspectives and new challenges. Ecancermedicalscience, 13, 961. [CrossRef]
4.  Tokumaru, Y., Joyce, D., Takabe, K. (2020). Current status and limitations of immunotherapy for breast cancer. Surgery, 167(3), 628-630. [CrossRef]

5.    Yu, L.Y., Tang, J., Zhang, C.M., Zeng, W.J., Yan, H., Li, M.P., Chen, X.P. (2017). New immunotherapy strategies in breast cancer. International Journal of Environmental Research and Public Health, 14(1), 68. [CrossRef]

6.    Chilakamarthi, U., Giribabu, L. (2017). Photodynamic therapy: Past, present and future. Chemical Record, 17(8), 775-802. [CrossRef]

7.    Kroschinsky, F., Stölzel, F., von Bonin, S., Beutel, G., Kochanek, M., Kiehl, M., Schellongowski, P. (2017). New drugs, new toxicities: Severe side effects of modern targeted and immunotherapy of cancer and their management. Critical Care, 21(1), 89. [CrossRef]

8.    Oun, R., Moussa, Y.E., Wheate, N.J. (2018). The side effects of platinum-based chemotherapy drugs: A review for chemists. Dalton Transactions, 47(19), 6645-6653. [CrossRef]

9.    Dos Santos, A.F., De Almeida, D.R.Q., Terra, L.F., Baptista, M.S., Labriola, L. (2019). Photodynamic therapy in cancer treatment-An update review. Journal of Cancer Metastasis and Treatment, 5, 25. [CrossRef]

10.   Hamblin, M.R. (2020). Photodynamic therapy for cancer: What's past is prologue. Photochemistry and Photobiology, 96(3), 506-516. [CrossRef]

11.   Liu, S., Feng, G., Tang, B.Z., Liu, B. (2021). Recent advances of AIE light-up probes for photodynamic therapy. Chemical Science, 12(19), 6488-6506. [CrossRef]

12.   Wang, S., Wu, W., Manghnani, P., Xu, S., Wang, Y., Goh, C.C., Ng, L.G., Liu, B. (2019). Polymerization-enhanced two-photon photosensitization for precise photodynamic therapy. ACS Nano, 13(3), 3095-3105. [CrossRef]

13.   Plotino, G., Grande, N.M., Mercade, M. (2019). Photodynamic therapy in endodontics. International Endodontic Journal, 52(6), 760-774. [CrossRef]

14.   Gunaydin, G., Gedik, M.E., Ayan, S. (2021). Photodynamic therapy-current limitations and novel approaches. Frontiers in Chemistry, 9, 691697. [CrossRef]

15.   Li, X., Wu, J., Wang, L., He, C., Chen, L., Jiao, Y., Duan, C. (2020). Mitochondrial-DNA-targeted IrIII - containing metallohelices with tunable photodynamic therapy efficacy in cancer cells. Angewandte Chemie (International Ed. in English), 59(16), 6420-6427. [CrossRef]

16.   Wan, Q., Zhang, R., Zhuang, Z., Li, Y., Huang, Y., Wang, Z., Zhang, W., Hou, J., Tang, B.Z. (2020). Molecular engineering to boost aie-active free radical photogenerators and enable high-performance photodynamic therapy under hypoxia. Advanced Functional Materials, 30(39), 1-12. [CrossRef]

17.   Allison, R.R., Moghissi, K. (2013). Photodynamic therapy (PDT): PDT mechanisms. Clinical Endoscopy, 46(1), 24-29. [CrossRef]

18.   Filatov, M.A. (2020). Heavy-atom-free BODIPY photosensitizers with intersystem crossing mediated by intramolecular photoinduced electron transfer. Organic and Biomolecular Chemistry, 18(1), 10–27. [CrossRef]

19.   Li, X., Lee, D., Huang, J.D., Yoon, J. (2018). Phthalocyanine-assembled nanodots as photosensitizers for highly efficient type I photoreactions in photodynamic therapy. Angewandte Chemie International Edition, 57(31), 9885-9890. [CrossRef]

20.   Chinna Ayya Swamy, P., Sivaraman, G., Priyanka, R.N., Raja, S.O., Ponnuvel, K., Shanmugpriya, J., Gulyani, A. (2020). Near Infrared (NIR) absorbing dyes as promising photosensitizer for photo dynamic therapy. Coordination Chemistry Reviews, 411, 213233. [CrossRef]

21.   Li, Y., Cai, Z., Liu, S., Zhang, H., Wong, S.T.H., Lam, J.W.Y., Kwok, R.T.K., Qian, J., Tang, B.Z. (2020). Design of AIEgens for near-infrared IIb imaging through structural modulation at molecular and morphological levels. Nature Communications, 11(1), 1255. [CrossRef]

22.   Chen, Y., Xue, L., Zhu, Q., Feng, Y., Wu, M. (2021). Recent advances in second near-infrared region (NIR-II) fluorophores and biomedical applications. Frontiers in Chemistry, 9, 750404. [CrossRef]

23.   He, B., Situ, B., Zhao, Z., Zheng, L. (2020). Promising applications of AIEgens in animal models. Small Methods, 4(4), 1900583. [CrossRef]

24.   He, S., Song, J., Qu, J., Cheng, Z. (2018). Crucial breakthrough of second near-infrared biological window fluorophores: Design and synthesis toward multimodal imaging and theranostics. Chemical Society Reviews, 47(12), 4258-4278. [CrossRef]

25.   Anthony, S.P. (2012). Organic solid-state fluorescence: Strategies for generating switchable and tunable fluorescent materials. ChemPlusChem, 77(7), 518-531. [CrossRef]

26.   Li, X., Jiang, M., Li, Y., Xue, Z., Zeng, S., Liu, H. (2019). 808 nm laser-triggered NIR-II emissive rare-earth nanoprobes for small tumor detection and blood vessel imaging. Materials Science and Engineering C, 100, 260-268. [CrossRef]

27.   Kenry, Duan, Y., Liu, B. (2018). Recent advances of optical imaging in the second near-infrared window. Advanced Materials, 30(47), 1-19. [CrossRef]

28.  Hu, C., Guo, T., Li, H., Xu, P., Xiao, Y. (2021). A novel NIR-II probe for improved tumor-targeting NIR-II imaging. RSC Advances, 11(62), 39287-39290. [CrossRef]

29.  Luo, C., Sun, B., Wang, C., Zhang, X., Chen, Y., Chen, Q., Yu, H., Zhao, H., Sun, M., Li, Z., Zhang, H., Kan, Q., Wang, Y., He, Z., Sun, J. (2019). Self-facilitated ROS-responsive nanoassembly of heterotypic dimer for synergistic chemo-photodynamic therapy. Journal of Controlled Release, 302, 79-89. [CrossRef]

30.  Li, Y., Liu, S., Ni, H., Zhang, H., Zhang, H., Chuah, C., Ma, C., Wong, K.S., Lam, J.W.Y., Kwok, R.T.K., Qian, J., Lu, X., Tang, B.Z. (2020). ACQ-to-AIE transformation: Tuning molecular packing by regioisomerization for two-photon NIR bioimaging. Angewandte Chemie, 132(31), 12922-12926. [CrossRef]

31.  Nie, H., Hu, K., Cai, Y., Peng, Q., Zhao, Z., Hu, R., Chen, J., Su, S.J., Qin, A., Tang, B.Z. (2017). Tetraphenylfuran: Aggregation-induced emission or aggregation-caused quenching? Materials Chemistry Frontiers, 1(6), 1125-1129. [CrossRef]

32.  Huang, Y., Xing, J., Gong, Q., Chen, L.C., Liu, G., Yao, C., Wang, Z., Zhang, H.L., Chen, Z., Zhang, Q. (2019). Reducing aggregation caused quenching effect through co-assembly of PAH chromophores and molecular barriers. Nature Communications, 10(1), 169. [CrossRef]

33.  Antaris, A.L., Chen, H., Cheng, K., Sun, Y., Hong, G., Qu, C., Diao, S., Deng, Z., Hu, X., Zhang, B., Zhang, X., Yaghi, O.K., Alamparambil, Z.R., Hong, X., Cheng, Z., Dai, H. (2016). A small-molecule dye for NIR-II imaging. Nature Materials, 15(2), 235-242. [CrossRef]

34.  Nguyen, V.N., Yan, Y., Zhao, J., Yoon, J. (2021). Heavy-atom-free photosensitizers: From molecular design to applications in the photodynamic therapy of cancer. Accounts of Chemical Research, 54(1), 207–220. [CrossRef]

35.  Xu, W., Wang, D., Tang, B.Z. (2020). NIR-II AIEgens: A win win integration towards bioapplications. Angewandte Chemie International Edition, 60(14), 7476-7487. [CrossRef]

36.  Xu, P., Kang, F., Yang, W., Zhang, M., Dang, R., Jiang, P., Wang, J. (2020). Molecular engineering of a high quantum yield NIR-II molecular fluorophore with aggregation-induced emission (AIE) characteristics for: *In vivo* imaging. Nanoscale, 12(8), 5084-5090. [CrossRef]

37.  Bhasikuttan, A.C., Mohanty, J., Nau, W.M., Pal, H. (2007). Efficient fluorescence enhancement and cooperative binding of an organic dye in a supra-biomolecular host–protein assembly. Angewandte Chemie International Edition, 46(22), 4120-4122. [CrossRef]

38.  Anees, P., Sreejith, S., Ajayaghosh, A. (2014). Self-assembled near-infrared dye nanoparticles as a selective protein sensor by activation of a dormant fluorophore. Journal of the American Chemical Society, 136(38), 13233-13239. [CrossRef]

39.  Jameson, L.P., Smith, N.W., Annunziata, O., Dzyuba, S.V. (2016). Interaction of BODIPY dyes with bovine serum albumin: A case study on the aggregation of a click-BODIPY dye. Physical Chemistry Chemical Physics, 18(21), 14182-14185. [CrossRef]

40.  Schneider, F., Ruhlandt, D., Gregor, I., Enderlein, J., Chizhik, A.I. (2017). Quantum yield measurements of fluorophores in lipid bilayers using a plasmonic nanocavity. The Journal of Physical Chemistry Letters, 8(7), 1472-1475. [CrossRef]

41.  Alifu, N., Zebibula, A., Qi, J., Zhang, H., Sun, C., Yu, X., Xue, D., Lam, J.W.Y., Li, G., Qian, J., Tang, B.Z. (2018). Single-molecular near-infrared-ii theranostic systems: Ultrastable aggregation-induced emission nanoparticles for long-term tracing and efficient photothermal therapy. ACS Nano, 12(11), 11282-11293. [CrossRef]

42.  Qi, J., Sun, C., Zebibula, A., Zhang, H., Kwok, R.T.K., Zhao, X., Xi, W., Lam, J.W.Y., Qian, J., Tang, B.Z. (2018). Real-time and high-resolution bioimaging with bright aggregation-induced emission dots in short-wave infrared region. Advanced Materials, 30(12), 1706856. [CrossRef]

43.  Qian, G., Zhong, Z., Luo, M., Yu, D., Zhang, Z., Ma, D., Wang, Z.Y. (2009). Synthesis and application of thiadiazoloquinoxaline-containing chromophores as dopants for efficient near-infrared organic light-emitting diodes. The Journal of Physical Chemistry C, 113(4), 1589-1595. [CrossRef]

44.  Moriguchi, I., Hirono, S., Nakagome, I., Hirano, H. (1994). Comparison of reliability of log p values for drugs calculated by several methods. Chemical and Pharmaceutical Bulletin, 42(4), 976-978. [CrossRef]

45.  Lipinski, C.A., Lombardo, F., Dominy, B.W., Feeney, P.J. (2001). Experimental and computational approaches to estimate solubility and permeability in drug discovery and development settings. Advanced Drug Delivery Reviews, 46(1-3), 3-26. [CrossRef]

46.  Daina, A., Michielin, O., Zoete, V. (2017). SwissADME: A free web tool to evaluate pharmacokinetics, drug-likeness and medicinal chemistry friendliness of small molecules. Scientific Reports, 7(1), 42717. [CrossRef]

47.  Ertl, P., Rohde, B., Selzer, P. (2000). Fast calculation of molecular polar surface area as a sum of fragment-

based contributions and its application to the prediction of drug transport properties. Journal of Medicinal Chemistry, 43(20), 3714-3717. [CrossRef]

48.  Coimbra, J.T.S., Feghali, R., Ribeiro, R.P., Ramos, M.J., Fernandes, P.A. (2020). The importance of intramolecular hydrogen bonds on the translocation of the small drug piracetam through a lipid bilayer. RSC Advances, 11(2), 899-908. [CrossRef]

49.  Khan, T., Dixit, S., Ahmad, R., Raza, S., Azad, I., Joshi, S., Khan, A.R. (2017). Molecular docking, PASS analysis, bioactivity score prediction, synthesis, characterization and biological activity evaluation of a functionalized 2-butanone thiosemicarbazone ligand and its complexes. Journal of Chemical Biology, 10(3), 91-104. [CrossRef]

50.  Dilly, S., Lamy, C., Marrion, N.V., Liégeois, J.F., Seutin, V. (2011). Ion-Channel Modulators: More diversity than previously thought. ChemBioChem, 12(12), 1808-1812. [CrossRef]

51.  Ferguson, F.M., Gray, N.S. (2018). Kinase inhibitors: The road ahead. Nature Reviews Drug Discovery, 17(5), 353-376. [CrossRef]

52.  Fischer, A., Smieško, M. (2019). Ligand pathways in nuclear receptors. Journal of Chemical Information and Modeling, 59(7), 3100-3109. [CrossRef]

53.  Puratchikody, A., Sriram, D., Umamaheswari, A., Irfan, N. (2016). 3-D structural interactions and quantitative structural toxicity studies of tyrosine derivatives intended for safe potent inflammation treatment. Chemistry Central Journal, 10(1), 1-19. [CrossRef]